

## Station 16.3: a High-Resolution Single-Crystal Diffraction Facility at the SRS, Daresbury

S. P. Collins,<sup>a\*</sup> R. J. Cernik,<sup>a</sup> B. Fell,<sup>a</sup> C. C. Tang,<sup>a</sup> N. W. Harris,<sup>a</sup> M. C. Miller<sup>a</sup> and G. Oszlanyi<sup>b</sup>

<sup>a</sup>CLRC Daresbury Laboratory, Warrington WA4 4AD, UK, and <sup>b</sup>Central Institute for Research in Physics, Budapest, Hungary. E-mail: s.p.collins@daresbury.ac.uk

(Received 6 February 1998; accepted 11 May 1998)

SRS station 16.3 is now a fully scheduled user facility for high-resolution and high-energy single-crystal X-ray diffraction. It is based on a large three-axis diffractometer, designed and constructed at Daresbury for a wide range of physics and materials science applications. Served by wiggler 16 (a 6 T superconducting wavelength-shifter), the station has access to a broad spectrum of photon energies, extending to over 50 keV, and is designed for simple polarization-state tuning by motorized height adjustment of all optical components. This paper outlines the key design features and some of the science projects carried out during the first year of operation.

**Keywords:** diffraction; diffractometers; magnetic diffraction; critical exponents; SRS station 16.3.

### 1. Background

In order to fill a significant gap in the facilities available at the SRS, station 16.3 was designed to meet two key criteria. First, the new station must provide instrumentation for high-resolution (triple-axis) single-crystal diffraction measurements using a wide range of photon energies, complementing existing diffractometer-based SRS facilities for crystal-structure determination (Cernik *et al.*, 1997), powder diffraction (Cernik *et al.*, 1990; Bushnell-Wye & Cernik, 1992) and surface science (Norris *et al.*, 1992). Second, and equally importantly, the adopted design must allow for far more flexibility than is typical of existing beamlines in order to encourage novel experiments and accommodate non-standard requirements from both the academic and industrial user communities.

A 6 T superconducting wavelength-shifter (wiggler 16) provides photon beams with a wide range of energies

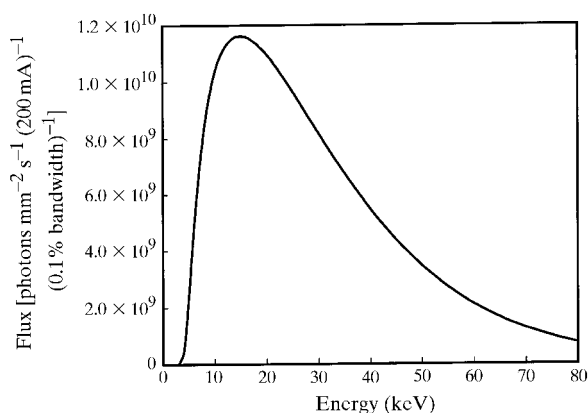


**Figure 1**

The calculated flux spectrum at station 16.3, sited 30 m from wiggler 16 on the SRS.

(Fig. 1) and, by adjusting slightly the vertical viewing angle, a range of polarization states from nearly linear to elliptical (Fig. 2). An important design decision *not* to employ focusing optics was taken early on, largely to preserve the beam polarization, collimation and energy range (at the expense of flux), although a focusing option is planned as a future upgrade.

### 2. Station design

The design of the most complex part of the station – the diffractometer – was governed by the following requirements:

(i) To utilize DC motors and angle encoders on all axes, ensuring high precision and accuracy with low electrical noise;

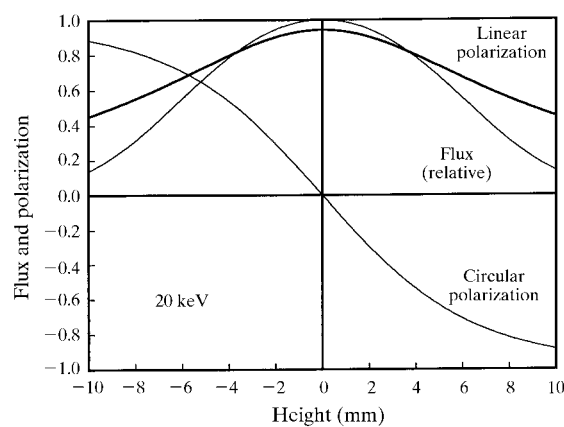


**Figure 2**

The variation in linear polarization, circular polarization and flux with height at station 16.3, calculated for a 20 keV X-ray beam.

**Table 1**

The accessible angular range, resolution (minimum step) and accuracy (largest angular error) for the diffractometer and monochromator axes.

A dash indicates no angular restrictions *without* ancillary equipment mounted.

Axis	Minimum angle (°)	Maximum angle (°)	Minimum step (°)	Accuracy (°)
$2\theta$ (primary arm)	-23	157	0.0001	0.0003
$\omega$ ( $\theta$ )	-	-	0.0001	0.0003
$\chi$ (Huber cradle)	-	-	1/38750	<0.008
$\varphi$ (Huber cradle)	-	-	0.0004	<0.008
Analyzer rotation	-	-	0.0001	0.0003
Secondary arm	-	-	1/77500	<0.005
Mono1	-10	50	0.0001	0.0003
Mono2	-	-	0.0001	0.0003

(ii) To employ a modified (DC/servo) version of the Huber 512 Eulerian cradle for versatility and 'standard' sample cell mounting;

(iii) To employ direct,  $10^{-4}$  deg resolution angle encoders on all critical axes;

(iv) To construct a robust primary detector arm with an integral heavy-duty analyzer stage and secondary detector arm;

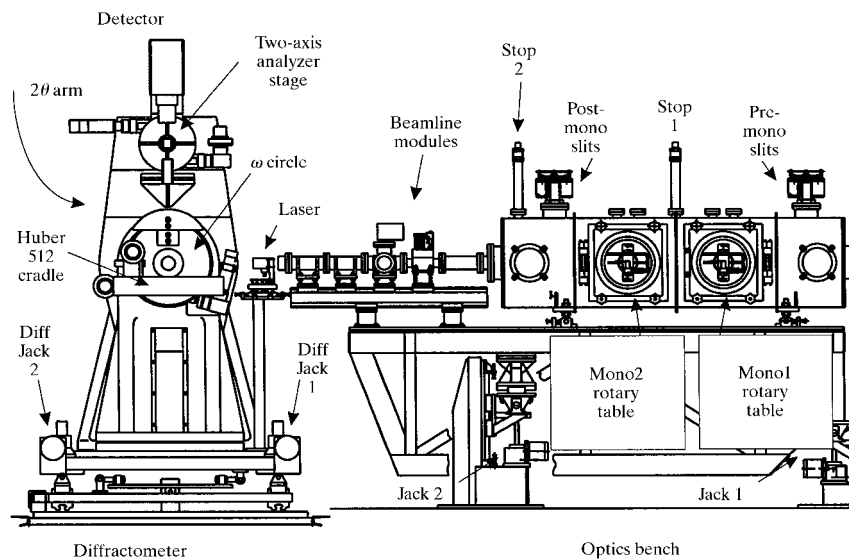
(v) To ensure that sample cells and detectors systems of moderate mass ( $\sim 10$  kg) can be employed without sacrificing either the arcsecond angular accuracy or sub-50  $\mu$ m sphere error.

The final design, illustrated in Fig. 3, was arrived at through a combination of finite-element-analysis calculations and prototype testing. The instrument satisfies all key design criteria, and is summarized as follows. A Franke 400 mm table provides the  $\omega$  (or  $\theta$ ) axis rotation by connecting the Eulerian cradle to a solid cast aluminium support, with a high-resolution Heidenhain ROD 800 angle encoder recording the rotation angle. A second solid

casting supports the primary detector arm – a partitioned hollow aluminium casting – using a similar rotary table/encoder combination for the  $2\theta$  axis, and providing a route for detector-arm cabling through the body of the diffractometer. The primary arm incorporates a double 250 mm rotary table, which rotates both the analyzer mount and the secondary detector arm. Some operational parameters for the diffractometer are given in Table 1.

As an aid to versatility, the diffractometer relies heavily on the use of standard commercial optical rails. X-95 components are employed to attach X-ray detectors to the secondary detector arm (the standard mounting position for all double- and triple-axis measurements) and to support a fixed sample alignment camera along the  $\omega/2\theta$  rotation axis. A similar optical bench arrangement sited downstream of the diffractometer holds instrumentation (e.g. an ionization chamber) used mainly to facilitate beam alignment. Where space is a major consideration, such as between the analyzer stage and cradle, compact X-26 rails are used to mount a range of detector and sample slit arrangements.

Upstream of the diffractometer (towards the source) lies an optics bench (Fig. 3) containing a monochromator vacuum vessel and associated instrumentation. Beamline optics are extremely simple. White beam enters the vacuum vessel and is monochromated by either one or two channel-cut crystals (or none for white-beam experiments) mounted on high-precision rotary table/encoder arrangements. The first monochromator is water-cooled, and all crystals are attached *via* standard mounting plates for rapid fitting and removal. An unusual feature of the beamline is the section between the monochromator vessel and diffractometer, which is constructed from a set of removable vacuum modules supported on another X-95 rail. These components perform various functions including beam intensity monitoring and remote foil insertion, and can be replaced

**Figure 3**

The station 16.3 diffractometer and optics bench.

by beam-conditioning modules for particular experiments, or removed completely to allow instrumentation to be mounted in air, directly onto the X-95 bench.

To take full advantage of the variation in polarization with vertical viewing angle, and to aid beam alignment, both the optics table and diffractometer can translate and tilt vertically under computer control. The diffractometer can also be translated horizontally, perpendicular to the beam direction.

### 3. Station software

Since the station instrumentation was designed with flexibility firmly in mind, similarly versatile software is clearly essential. The data-acquisition system must be simple to use while placing no additional constraints on the experimental strategy. Our solution is the combination of *PINCER* (a general-purpose command interpreter, see Miller *et al.*, 1992) and a macro library (*CLAM*), both of which will be

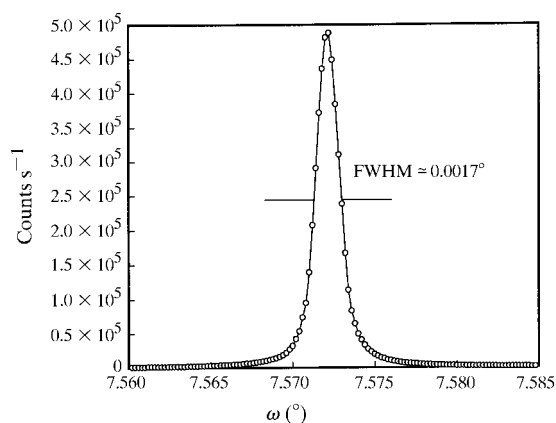


**Figure 4**  
A double-axis  $\theta/2\theta$  scan with Si(111) sample and monochromator reflections.

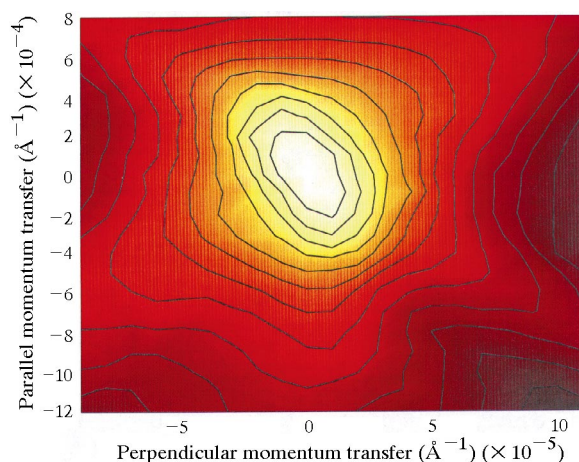


**Figure 5**  
A triple-axis momentum-transfer map around the Si(111) sample reflection, using a double-bounce Si(111) monochromator and analyzer combination. The innermost contour represents the FWHM, with each subsequent contour indicating a further halving of intensity.

described in detail in a separate publication. Briefly, the *CLAM* library provides a uniform interface to *all* hardware control *via* a set of virtual motor macros. Simple (scalar) motors can be controlled (moved, scanned *etc.*) in a conventional manner. However, the same compact set of functions can also be used to perform far more complex tasks, including the control of vector (multiple input/output) devices such as multichannel analyzers and reciprocal space positioning, using an identical command syntax.

### 4. Science areas

During the first year of scheduled operation, a wide range of projects have been successfully completed on the station. These include high-resolution studies of lattice distortions and dislocations (Kowalski *et al.*, 1996), charge-density waves, charge ordering (Su *et al.*, 1998), multilayer diffraction, magnetic diffraction (Collins *et al.*, 1996), circular dichroism, linear dichroism (Collins, 1997), high-resolution powder diffraction (Maginn, 1998), reflectivity, residual strain mapping, topography and multiple diffrac-

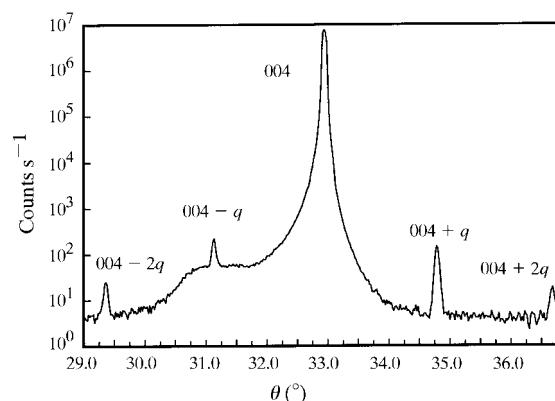


**Figure 6**  
The strong Ho (004) charge reflection with four resonant ( $L_3$ -edge) magnetic satellite peaks.

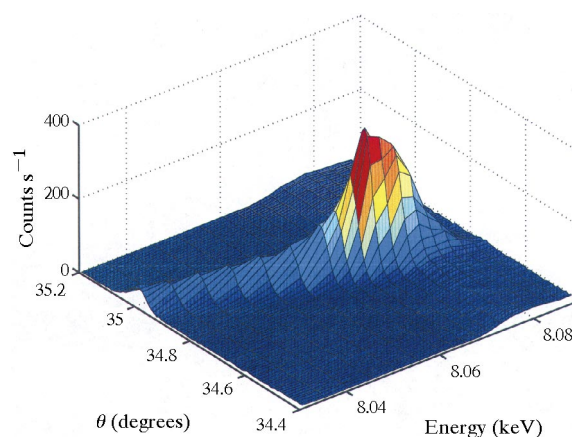


**Figure 7**  
The Ho (004 +  $q$ ) satellite reflection as a function of photon energy (no correction has been applied for sample absorption, which increases by around a factor of three above the edge).

tion (Morelhão *et al.*, 1998). By way of illustration, a few examples of early measurements are reproduced here.

The first of these is high-resolution room-temperature diffraction from a silicon crystal taken with the standard detector, a Bede EDRA (maximum count rate  $\sim 2 \times 10^6$  counts  $s^{-1}$ ). Fig. 4 shows an Si(111)  $\theta/2\theta$  scan (in two-axis mode) taken at 15 keV. The total angular width, to which the sample and instrument make comparable contributions, is around 1.7 mdeg (6 arcsec). A two-dimensional momentum-transfer map of the same reflection, this time using an Si(111) double-bounce analyzer, is illustrated in Fig. 5. The peak half-widths parallel and

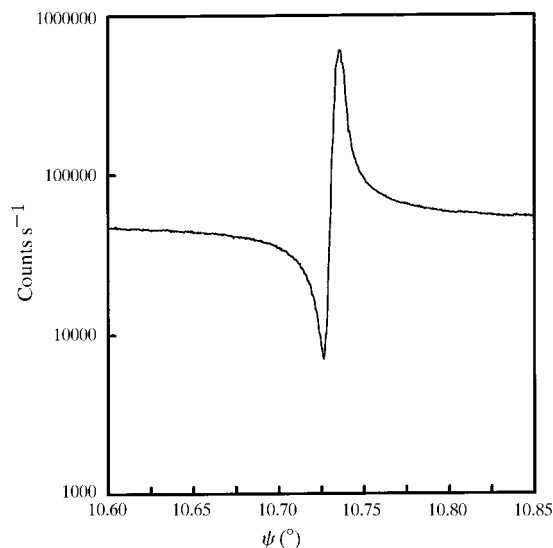


**Figure 8**

Part of a  $\psi$  scan around the Si(222) setting, illustrating constructive and destructive interference between single and multiple diffraction.

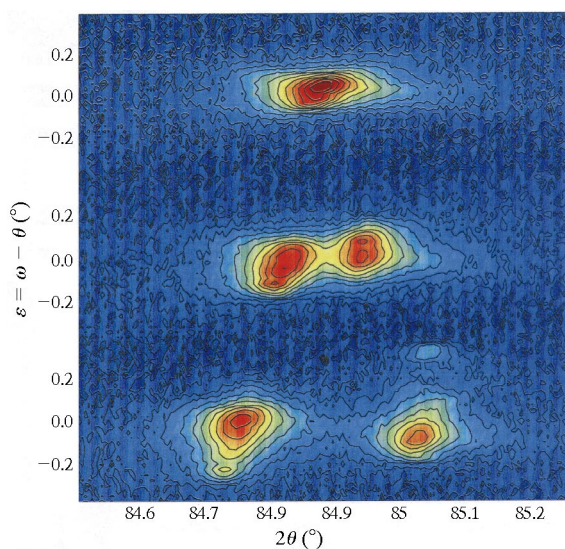


**Figure 9**

Grid scans of  $2\theta$  versus  $\varepsilon = \omega - \theta$  around the uranium sulfide (840) reflection close to the magnetic phase transition. The plots are offset vertically for clarity, and correspond to temperatures of 185 K (top), 175 K (centre) and 160 K (bottom).

perpendicular to the direction of momentum transfer (represented by the innermost contour) are around  $3.9 \times 10^{-4} \text{ \AA}^{-1}$  and  $2.5 \times 10^{-5} \text{ \AA}^{-1}$ , respectively (the momentum transfer is in units of  $4\pi \sin\theta/\lambda$ ). Instrumental 'streaks', visible in the low-intensity contours, are largely suppressed by the double-bounce monochromator and analyzer.

A second example from station 16.3 is resonant magnetic diffraction from antiferromagnetic holmium. These measurements (Collins *et al.*, 1996) were performed at a temperature of 30 K by mounting a Displex cryostat (10–300 K) onto the Eulerian cradle and using a germanium solid-state detector to remove much of the background fluorescence signal from the weak resonant elastic scattering. The incommensurate spiral magnetic structure of holmium (Gibbs *et al.*, 1991; Tang *et al.*, 1992) leads to a series of resonant harmonic satellite reflections surrounding each charge peak. The weakness of these reflections, even close to the holmium  $L_3$  absorption edge where the resonance enhancement is greatest, is clear from Fig. 6. (The strong charge peak was measured with a very small beam size and re-scaled to avoid saturating the solid-state detector, which has a maximum count rate of around  $10^5$  counts  $s^{-1}$ .) To illustrate the resonant nature of the magnetic reflections, the  $(004 + q)$  satellite is shown in Fig. 7 as a function of energy. Note the highly asymmetric resonant profile, which is due to constructive and destructive interference combined with a change in sample absorption across the  $L_3$  edge of around a factor of three.

Of growing interest in recent years is the measurement of multiple diffraction, or the Renninger effect. This technique, which will be the subject of a separate paper, has proved to be invaluable for a diversity of studies, ranging from small lattice distortions to phase determination in diffraction. Again, the combination of high-quality hardware and versatile software allows such measurements to be performed with ease, requiring no special sample

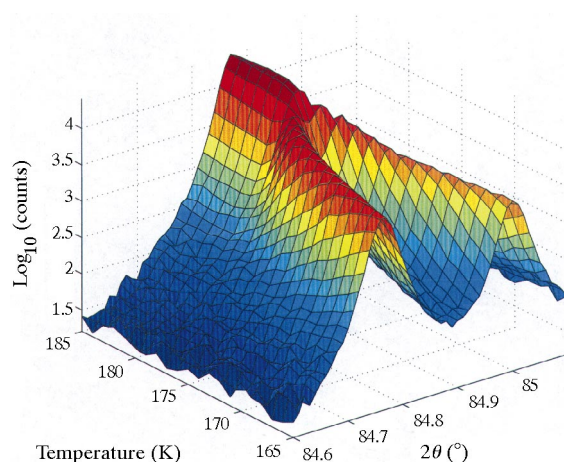


**Figure 10**

Splitting of the (840) Bragg reflection in US versus temperature. The sample was rocked about the  $\omega$  axis at each scan point to provide integrated intensities.

mounting. An example of part of a  $\psi$  scan around the (222) reflection of silicon is shown in Fig. 8.

## 5. Magnetostriction in uranium sulfide

The final example of experimental data collected on station 16.3 concerns the magnetically induced cubic-to-rhombohedral lattice distortion in ferromagnetic uranium sulfide as the crystal is cooled through its Curie temperature of around 180 K with no applied field. The splitting of the (840) Bragg peak is clearly illustrated in a set of three grid scans of  $2\theta$  versus  $\varepsilon = \omega - \theta$  (departure from the bisecting condition), shown in Fig. 9, which map out an area of reciprocal space around the reflection at various temperatures close to the phase transition. It is interesting to note that, while the peaks split along the direction of momentum transfer (reflecting a well defined change in  $d$ -spacing), the main effect along the orthogonal direction is a broadening of the peaks. The change in  $d$ -spacing with temperature is relatively straightforward to interpret, and is discussed here.

In order to avoid making lengthy grid scans at a large number of temperatures, a series of  $2\theta$  scans were performed, as a function of temperature, by rocking the  $\omega$  axis over a suitable range. Such measurements were carried out very easily with the *CLAM* macro library and a virtual motor to rock  $\omega$  about the current position and integrate detector counts at each point. Fig. 10 shows the measured peak splitting with temperature.

A small rhombohedral distortion to the cubic unit cell with no volume change leads to the (840) Bragg peak splitting into a doublet, with a separation (see Appendix A) of

$$\Delta(2\theta)/\tan(2\theta) = 4\delta/5, \quad (1)$$

where the rhombohedral cell angles are  $(\pi/2 + \delta)$  with  $|\delta| \ll 1$ . The power-law temperature dependence of the lattice strain is characterized (Bruce, 1980) by

$$\delta \propto |t|^{\tilde{\beta}}, \quad (2)$$

where  $t = (T - T_c)/T_c$  is the reduced temperature for a Curie temperature of  $T_c$ . This is analogous to the more familiar magnetization variation (see, for example, Collins, 1989),

$$M \propto |t|^{\beta}. \quad (3)$$

One would expect the critical exponents  $\beta$  and  $\tilde{\beta}$  to be related (since the magnetization *causes* the strain). Indeed, Marples (1970) showed, from an analysis of neutron powder diffraction and magnetization data, that  $\delta \propto M^2$  (implying that  $\tilde{\beta} = 2\beta$ ), exactly as predicted by mean-field theory. Moreover, the assignment (Tillwick & Plessis, 1976) of  $\beta = 0.55 \pm 0.05$  agrees well with the mean-field value  $\beta = 0.5$ .

The critical exponent for lattice strain measured in the present work, extracted from the diffraction scans by first fitting the  $2\theta$  peaks to pairs of pseudo-Voigt functions and

then fitting the resulting peak centres to a power law (see Fig. 11), is the remarkably precise value of  $\tilde{\beta} = 0.500 \pm 0.005$  with  $T_c = 178.65 \pm 0.03$  K. (Note that the uncertainty in  $T_c$  neglects any systematic errors in the temperature calibration, which may be significantly larger than the standard deviations due to random errors given above). This result is clearly inconsistent, by exactly a factor of two, with the mean-field value of  $\tilde{\beta} = 1$ . While detailed renormalization-group analyses predict a more complex relationship between  $\beta$  and  $\tilde{\beta}$ , their ratio tends not to depart *dramatically* from the mean-field value of 0.5. For example, with a perturbed 3d Heisenberg magnet one expects (Bruce, 1980)  $\beta = 0.37$ ,  $\tilde{\beta} = 0.85$ . (Notice that, unlike the present analysis,  $\tilde{\beta} \geq 2\beta$ .)

The origin of the large disparity between  $\tilde{\beta}$  and  $2\beta$  in US is far from clear. Further experimental evaluation of  $\tilde{\beta}$  might prove useful, especially since the magnetization exponent for US appears to be uncharacteristically high compared with those of neighbouring uranium chalcogenides (Collins, 1989). A more intriguing possibility is that the critical exponent extracted from diffraction of an X-ray beam, which penetrates just a few micrometres into the material, is different from that of the bulk. Such 'near surface' effects have been observed in other measurements (Thurston *et al.*, 1993), and might explain why (highly penetrating) neutron diffraction results appear to conflict with the X-ray data.

## 6. Summary

Station 16.3, designed primarily for high-resolution and high-energy single-crystal diffraction, is a very versatile facility, able to accommodate a wide range of scientific activities. Energy and polarization are easily tuneable,

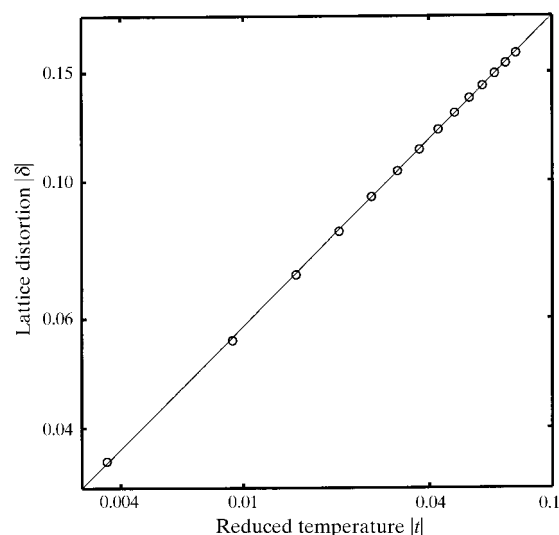


**Figure 11**

A log-log plot of the lattice distortion  $|\delta|$  versus reduced temperature. Power-law behaviour is confirmed by the points lying precisely on a straight line.

monochromators may be changed with ease, and modular beamline components may be moved in and out as required. A similar philosophy for software design has produced a simple but very powerful system for data acquisition and instrument control, which is well matched to the requirements of the new station.

## APPENDIX A

Here, we derive equation (1) by considering the relationship between the  $2\theta$  peak splitting and the lattice distortion  $\delta$ . To this end, it is useful to employ the metric tensor (see, for example, Sands, 1982) of the lattice.

A cubic lattice of side  $a$  has the metric tensor,

$$\mathbf{g}_0 = a^2 \begin{pmatrix} 1 & 0 & 0 \\ 0 & 1 & 0 \\ 0 & 0 & 1 \end{pmatrix} = a^2 \mathbf{I}, \quad (4)$$

in terms of which one can deduce the length,  $q_0$ , of the reciprocal lattice vector

$$\mathbf{h} = \begin{pmatrix} h \\ k \\ l \end{pmatrix}$$

using the relationship

$$q_0^2 = (2\pi)^2 \mathbf{h}'(\mathbf{g}_0^*)\mathbf{h}. \quad (5)$$

Here,  $\mathbf{g}_0^*$  is the reciprocal metric tensor, which for a cubic lattice is simply  $\mathbf{g}_0^* = a^{-2}\mathbf{I}$ . For a weakly distorted cubic lattice with a rhombohedral cell angle  $\alpha = \beta = \gamma = \pi/2 + \delta$  and  $|\delta| \ll 1$  ( $\delta$  may be positive or negative), one can write

$$\begin{aligned} \mathbf{g}_1 &= a^2 \begin{bmatrix} 1 & \cos(\pi/2 + \delta) & \cos(\pi/2 + \delta) \\ \cos(\pi/2 + \delta) & 1 & \cos(\pi/2 + \delta) \\ \cos(\pi/2 + \delta) & \cos(\pi/2 + \delta) & 1 \end{bmatrix} \\ &\simeq a^2 \begin{pmatrix} 1 & -\delta & -\delta \\ -\delta & 1 & -\delta \\ -\delta & -\delta & 1 \end{pmatrix}, \\ \mathbf{g}_1^* &\simeq \frac{1}{a^2} \begin{pmatrix} 1 & \delta & \delta \\ \delta & 1 & \delta \\ \delta & \delta & 1 \end{pmatrix}. \end{aligned} \quad (6)$$

Rearranging the above expressions for a small lattice distortion gives, to first order,

$$\Delta q/q_0 \simeq \mathbf{h}'(\mathbf{g}_1^* - \mathbf{g}_0^*)\mathbf{h}/[2\mathbf{h}'(\mathbf{g}_0^*)\mathbf{h}], \quad (7)$$

where  $\Delta q = q_1 - q_0$ . Inserting

$$\mathbf{h} = \begin{pmatrix} 2k \\ k \\ 0 \end{pmatrix}$$

into (7) one obtains a fractional change in momentum transfer of

$$\Delta q/q_0 = 2\delta/5. \quad (8)$$

The above expression represents the momentum-transfer shift for a lattice which is contracted ( $\delta > 0$ ) or expanded

( $\delta < 0$ ) along  $[111]$  as a result, in the present case, of magnetic ordering along the  $[111]$  or  $[\bar{1}\bar{1}\bar{1}]$  vectors. In an unmagnetized sample, one would expect a roughly uniform distribution of domains with distortions along  $[111]$ ,  $[\bar{1}\bar{1}\bar{1}]$ ,  $[1\bar{1}\bar{1}]$  and  $[\bar{1}\bar{1}1]$  with the corresponding set of reciprocal metric tensors,

$$\begin{aligned} \mathbf{g}_1^* &= \frac{1}{a^2} \begin{pmatrix} 1 & \delta & \delta \\ \delta & 1 & \delta \\ \delta & \delta & 1 \end{pmatrix}, \frac{1}{a^2} \begin{pmatrix} 1 & -\delta & -\delta \\ -\delta & 1 & \delta \\ -\delta & \delta & 1 \end{pmatrix}, \\ &\frac{1}{a^2} \begin{pmatrix} 1 & -\delta & \delta \\ -\delta & 1 & -\delta \\ \delta & -\delta & 1 \end{pmatrix}, \frac{1}{a^2} \begin{pmatrix} 1 & \delta & -\delta \\ \delta & 1 & -\delta \\ -\delta & -\delta & 1 \end{pmatrix}. \end{aligned} \quad (9)$$

Inserting these into (7) for a  $(2k, k, 0)$  reflection leads to two distinct values of momentum transfer (hence a double peak), with a splitting

$$\pm \Delta q/q_0 = 4\delta/5, \quad (10)$$

which is sensitive to the magnitude, but not the sign, of  $\delta$ . Finally, the fractional change in momentum transfer is related to the  $2\theta$  splitting via Bragg's law, and we reproduce the result in equation (1):

$$\Delta(2\theta)/\tan(2\theta) = 4\delta/5.$$

The authors are indebted to Professor W. G. Stirling for helpful discussions and the loan of the holmium crystal, Professor J. B. Forsyth for valuable comments on instrumentation and software design, Professor G. H. Lander and Professor O. Vogt for providing the US crystal, Dr D. Laundy for calculations of the X-ray beam parameters, Professor R. A. Cowley for guidance on critical exponents, and Professor W. Clegg for checking the manuscript.

## References

- Bruce, A. D. (1980). *Adv. Phys.* **29**, 111–219.  
 Bushnell-Wye, G. & Cernik, R. J. (1992). *Rev. Sci. Instrum.* **63**, 999–1001.  
 Cernik, R. J., Clegg, W., Catlow, C. R. A., Bushnell-Wye, G., Flaherty, J. V., Greaves, G. N., Burrows, I., Taylor, D. J., Teat, S. J. & Hamichi, M. (1997). *J. Synchrotron Rad.* **4**, 279–286.  
 Cernik, R. J., Murray, P. K., Pattison, P. & Fitch, A. N. (1990). *Appl. Cryst.* **23**, 292–296.  
 Collins, M. F. (1989). *Magnetic Critical Scattering*. Oxford University Press.  
 Collins, S. P. (1997). *Nucl. Instrum. Methods*, **B129**, 289–296.  
 Collins, S. P., Tang, C. C., Stirling, W. G. & Longfield, M. (1996). *Daresbury Laboratory Scientific Report 1995–1996 (Synchrotron Radiation Department)*. Daresbury Laboratory, Warrington WA4 4AD, UK.  
 Gibbs, D., Grubel, G., Harshman, D. R., Isaacs, E. D., McWhan, D. B., Mills, D. & Vettier, C. (1991). *Phys. Rev. B*, **43**, 5663–5681.  
 Kowalski, G., Moore, M. & Collins, S. P. (1996). *Daresbury Laboratory Annual Report 1995–1996 (Synchrotron Radiation Department)*, pp. 32–33. Daresbury Laboratory, Warrington WA4 4AD, UK.  
 Maginn, S. J. (1998). *Analyst*, **123**, 19R–29R.  
 Marples, J. A. C. (1970). *J. Phys. Chem. Solids*, **31**, 2431–2439.

- Miller, M. C., Ackroyd, K. & Oszlanyi, G. (1992). Preprint DL/CSE/P29E. Daresbury Laboratory, Warrington WA4 4AD, UK.
- Morelhão, S. L., Avanci, L. H., Hayashi, M. A., Cardoso, L. P. & Collins, S. P. (1998). *Appl. Phys. Lett.* Accepted.
- Norris, C., Finney, M. S., Clark, G. F., Baker, G., Moore, P. R. & van Silfhout, R. (1992). *Rev. Sci. Instrum.* **63**, 1083–1086.
- Sands, D. E. (1982). *Vectors and Tensors in Crystallography*. Reading, MA: Addison-Wesley.
- Su, Y., Du, C.-H., Tanner, B. K., Hatton, P. D., Collins, S. P., Brown, S., Paul, D. F. & Cheong, S. W. (1998). *J. Supercond.* Accepted.
- Tang, C. C., Stirling, W. G., Jones, D. L., Wilson, C. C., Haycock, P. W., Rollason, A. J., Thomas, A. H. & Fort, D. (1992). *J. Magn. Magn. Matter*, **103**, 86–96.
- Thurston, T. R., Helgesen, G., Gibbs, D., Hill, J. P., Gaulin, B. D. & Shirane, G. (1993). *Phys. Rev. Lett.* **70**, 3151–3154.
- Tillwick, D. L. & du Plessis, P. de V. (1976). *J. Magn. Magn. Matter*, **3**, 319–328.